

Shape-shifting nanoparticles on a perovskite oxide for highly stable and active heterogeneous catalysis

Yo Han Kim^a, Youngho Kang^a, Seung Yeon Jo^a, Hyun Gwon Jeong^a, Dragos Neagu^{b,*} and Jae-ha Myung^{a,*}

^a*Department of Materials Science and Engineering, Incheon National University, Incheon, 22012, Republic of Korea*

^b*Department of Chemical and Process Engineering, University of Strathclyde, Glasgow, G1 1XL, UK*

* Correspondence should be addressed to dragos.naegu@strath.ac.uk and mjaeha@inu.ac.kr

Abstract

Controlling the geometric shape of nano-catalysts plays a key role in obtaining unique properties of catalysts. Although shape control of nanoparticles is well known by various preparation methods, still there is no clear case for exsolution. Here we show that the shape of exsolved Ni nanoparticles can be changed during particle growth, by controlling reduction temperature and time. To elucidate and generalize the shape evolution, we develop a model which describes the equilibrium shape of nanoparticles on support thermodynamically. Our results suggest that there is a thermodynamic driving force for the exsolved nanoparticle to be stabilized into faceted shape with low surface/interface energy, during the exsolution process. Through catalytic activity testing, the improved durability of shape-evolved Ni catalysts was confirmed on dry-reforming condition over 390 hours, resulting from enhanced interface stability and coking resistance. This provides theoretical and experimental framework for the shape control of exsolved particle on oxide support, but also for the design of unique catalyst with high stability and reactivity.

Introduction

The in-situ exsolution, a type of controlled phase separation, has attracted much attention as an innovative way to uniformly form metallic nanoparticles from oxide lattices (mostly perovskites), at their surface, by the simple process of exposure to reducing environments, at high temperatures. Furthermore, the nanoparticles exsolved on oxide supports can exhibit not only high catalytic activity, but also unique stability for carbon coking, impurity poisoning and agglomeration at high temperature due to their uniform particle dispersion and strong adhesion

between metallic particle and oxide support^{1,2}. Whereby, such exsolved materials have been intensively exploited in various areas such as catalysis and electrochemistry for energy conversion and storage including reforming of methane³, CO oxidation⁴, NO_x conversion⁵, water splitting⁶, solid oxide cells (SOCs)^{7–11}, chemical looping¹² and Li-air battery¹³.

Controlling nanoparticle shape has become routine and expected for various nanoparticles preparation methods, although this is yet to be the case for exsolution. As an example, the shape of free particles prepared by colloidal method can be turned into polyhedron via controlling certain capping reagents (e.g. Poly vinyl pyrrolidone) and their molar ratio¹⁴. To date, exsolution studies have been focused on controlling chemical composition, size and number of exsolved particle by adjusting chemical and crystallographic properties of oxide parent (stoichiometry¹⁵, crystallographic orientation¹⁶ and termination¹⁷) and reduction condition (reduction temperature¹², reduction time¹⁸, Po₂¹⁹ and electrochemical potential⁷) to tune the performance of the nano-catalyst. In stark contrast, very little has been done to understand and control the shape of exsolved nanoparticles, even though this is a critical aspect of their application and functionality. There are currently only two studies that touch on these aspects, one²⁰ revealing that exsolved nanoparticles are generally quasi-spherical and partly submerged (socketed in the support), i.e., without specific facet orientation, and the second indicating that²¹ cubic-shaped exsolved nanoparticles may form during reduction in a CO atmosphere. However, the underlying mechanism for shape evolution and their direct control remains largely unexplored and unclear.

Herein, we investigate the shape evolution of Ni nanoparticles during exsolution, from a perovskite system, under H₂ environment, in a wide temperature range of 600–1000 °C. Morphological and structural analysis using microscopy clearly shows that the exsolved particles, initially spherical, gradually evolves to a faceted surface/interface with low-index plane including stable {100} and {111} facet during particle growth, with maintaining strict crystallographic relationships with the support. The shape evolution mechanism was thermodynamically elucidated by developed a model as function of the free energies of bulk, surface and interface. The shape-evolved Ni catalysts with stabilized facets exhibit superior and continuous catalytic activity on harsh hydrocarbon dry-reforming condition compared to spherical Ni exsolution and reference catalysts. Our results show that particle growth on exsolution can be vital in controlling surface and interface, and can provide a pathway for design of supported nano-catalyst with prominent activity and stability.

Results and discussion

System design and exsolution.

In order to achieve the Ni exsolution, a Ni-doped titanate perovskite oxide material was designed, being expected to show high structure tolerance for doping and redox environment at high temperatures¹². In addition, the A-site deficient perovskite structure was used, which enhances the exsolution tendency by providing driving force for B-site exsolution¹⁵. A La-rich (La, Ca) perovskite lattice was also employed, because, as observed in our own studies here and consistent with previous observations¹, this enhances the extent of exsolution, leading to larger nanoparticles, for which shape is easier to resolve in detail. (**Supplementary Fig. 1** for composition development and selection). Furthermore, the composition needs to present a substantial Ni surface segregation energy which was probed by DFT calculations. Based on the considerations above, our designed composition is $\text{La}_{0.7}\text{Ca}_{0.2}\text{Ni}_{0.25}\text{Ti}_{0.75}\text{O}_3$ (LCNT). This was successfully prepared by solid-state reaction (**Supplementary Fig. 2, 3** and **Supplementary Table 1** for morphology and phase analysis). Our density functional theory (DFT) calculations on the designed LCNT show large negative values of the surface segregation energy of -0.51 and -0.44 eV for Ni and Ni- V_{O} , respectively, implying good propensity towards Ni exsolution (**Supplementary Fig. 4**).

To verify the exsolution trends, the LCNT pellets were preheated under various reduction condition (in dry H_2 at $600 - 1000$ °C for 3 h and 24 h). The pristine LCNT surface shows clean and smooth morphology (**Supplementary Fig. 2a**). After reduction, the uniformly dispersed nanoparticles were observed on the surface via exsolution. As reduction temperature and time increase, the average size of exsolved particles on reduced LCNT becomes bigger (**Fig. 1a, b and Table 1**). This suggests that the particle growth on exsolution process could be controlled by reduction temperature and time, corresponding with increasing molar ratio of Ni-phase with increasing reduction temperature and time in phase analysis (**Fig. 1c and Supplementary Fig. 3**).

Shape observation and evolution.

In numerous reports for particle exsolution^{1,2,12,13,15-22,3,23-27,4,6-11}, the shape of exsolved particles has been formed into partly-embedded quasi-sphere. In this system, the spherical shape of particle was also observed after reduction at $600 - 800$ °C. However, interestingly, distinct polyhedral shapes, i.e. having faceted surface were observed at

larger particle sizes (over 50 nm) after reduction at high temperatures of 900 – 1000 °C (**Fig. 1 a and b**). When comparing the shapes of particles grown at 900 °C for 3 h and 24 h, it becomes apparent that the initial quasi-spherical particle shape has evolved into polyhedron-shaped particle. A very important aspect to note, however, is that similar shapes observed adjacently also seem to have the same alignment. This implies that they share crystallographic alignment with the support, growing epitaxially during exsolution, and thus the shape and orientation of the exsolved nanoparticles is strongly determined by surface orientation of the perovskite support on which it grows. This is a very important observation because it shows that even as the particles grow larger, exsolution remains a controlled segregation process, and the nanoparticles still maintain strict crystallographic relationship with the support. In addition, this shows that the shape, size and population density of particles depends on orientation of support due to surface facet-dependence on exsolution process^{15,16}.

We further investigated the evolution of the particle shape using High-Voltage Transmission Electron Microscopy (HVEM), which can provide atomic scale resolution on even relatively thick sample (over 150 nm) via high acceleration voltage electron beam. To prepare TEM samples for observing exsolved particle with different size, LCNT powders and pellets were reduced in various reduction conditions focusing on the conditions where shape evolution seems to begin to take place (e.g. 800 °C for 24 h and at 900 °C for 3h, 24 h). Representative cross-sections of the exsolved nanoparticles were obtained by extracting lamella samples of the above-mentioned sample by milling/focus ion beam (FIB), which were then analyzed by HVEM. **Fig. 2** shows the HVEM image of exsolved Ni nanoparticles with different size (20, 61, 81, 102 and 140 nm in order). All exsolved particles were single Ni metal and epitaxial with respect to LCNT support (**Supplementary Fig. 5**). As the particle size increase, the embedded sphere-shaped particle was turned into polyhedral particle and note that not only its surface becomes more faceted, but also its interface with the perovskite, while maintaining some degree of socketing. Since, as shown above, the perovskite support dictates the growth and orientation of the nanoparticles through epitaxy, it is worth investigating the contact planes between the perovskite and nanoparticle during this evolution. As seen in **Fig. 2**, upon increasing particle size, the interface between Ni and LCNT largely consists of {100} and {111} orientations. Then, the surface of the Ni particle is generally faceted with mostly {111} orientation. The prominence of the {111} orientation can be better understood by considering the relative energy of metal facets. In a previous study, the surface energies of Ni have been estimated by experiment and calculation within general gradient approximations (GGA)²⁸. The calculated surface energy of (111) facet (1.93 J/m²) was lower than that of

(100) facet (2.19 J/m²), (110) facet (2.25 J/m²) and experimental value of polycrystal (2.45 J/m²). Additionally, (111) is also regarded as generally the most stable crystalline plane in FCC metal²⁹. Therefore, the most stable (111) facet could be preferentially formed on the surface of exsolved Ni particles during growth to minimize the free surface energy. There were the various shapes of (111)-faceted Ni particles socketed on different surface including (100) and (111), as shown in **Supplementary Fig. 6 and 7**.

Energetics of shape evolution.

As mentioned above, the exsolved particles have generally been described as spheres partly-embedded in the oxide surface^{1,16}. However, our observations here are that, as the particle grows, there is tendency to adopt more polyhedral shapes, with more stable, low-index surfaces and interfaces. Generally, polyhedral shapes have larger surface than spherical particles having the same volume³⁰. For example, considering a sphere and a dodecahedron of same volume, the sphere has about 90% of surface area of the dodecahedron. This suggests that when the exsolved particles become polyhedral, they tend to increase their interface area, as opposed to the common behavior (e.g. in deposited particles) of reducing their surface area to minimize surface free energy. In ‘wetting’ state, which seems to be occurring here due to the consistently observed particle-substrate epitaxy, the interfacial energy (γ_{int}^*) between the nanocrystal and oxide substrate could be lower than the surface energy of nanocrystal³¹⁻³³, probably favored by the chemical and physical adhesion between nanoparticle and support.

To understand the variation of exsolution behavior depending on particle size, we consider the free energy model for the Ni exsolution (ΔG_{ex}) as follows:

$$\Delta G_{ex} = V^{Ni} \Delta g_{form}^{Ni} + V_{eli}^{LCNT} \Delta g_{eli}^{LCNT} + A_{surf}^{Ni} \gamma_{surf}^{Ni} - A_{surf}^{LCNT} \gamma_{surf}^{LCNT} + A_{int} \gamma_{int}, \quad (1)$$

where V^{Ni} is the volume of a Ni particle and Δg_{form}^{Ni} is the energy gain per unit volume due to the formation of the pure Ni phase. V_{eli}^{Ni} is the volume of the LCNT bulk that is eliminated due to the embedment of the particle and Δg_{eli}^{LCNT} is the volumetric free energy change associated with the dissociation of chemical bonds of LCNT. A_{surf}^{Ni} and A_{surf}^{LCNT} are the areas of the Ni and LCNT surfaces that are created and removed during the exsolution process, respectively, and γ_{surf}^{Ni} and γ_{surf}^{LCNT} are the corresponding surface energies. A_{int} is the area of the Ni-LCNT interface introduced by the formation of the Ni particle and γ_{int} is the interfacial energy. Because of the area dependence of the last three terms, their summation (ΔG_{area}^*) can be rewritten as:

$$\Delta G_{\text{area}}^* = A_{\text{surf}}^{\text{Ni}} \gamma_{\text{surf}}^{\text{Ni}} - A_{\text{surf}}^{\text{LCNT}} \gamma_{\text{surf}}^{\text{LCNT}} + A_{\text{int}} \gamma_{\text{int}} = \alpha_{\text{shape}} (V^{\text{Ni}})^{\frac{2}{3}}, \quad (2)$$

where α_{shape} denotes the shape factor that determines the effect of surface/interface energies and structures on particle shape (see below)³³. In **eq. (1)**, the $V^{\text{Ni}} \Delta g_{\text{form}}^{\text{Ni}}$ is a main thermodynamic incentive that enables the exsolution of Ni particles. Meanwhile, the others constitute constraints that regulate the degree of embedment and particle shape.

As observed above, low-temperature exsolutions yield a large number of small spherical particles that are partly embedded into the host. The spherical shape of the particles is probably favored because the sphere is a three-dimensional structure with the smallest surface-to-volume ratio, thus minimizing the free surface energy of a small-particle system. Since the surface energy is usually greater than the interface energy (more ‘dangling bonds’ at the surface, i.e., $\gamma_{\text{surf}}^{\text{Ni}} > \gamma_{\text{int}}$), embedded particles would thus be energetically more advantageous over more ‘wetting’, polyhedral ones, because the former has a lower interface-to-surface area ratio. However, the embedment of the particles entails an increase of the free energy of the system due to the removal of a part of the LCNT bulk ($V_{\text{eli}}^{\text{LCNT}} \Delta g_{\text{eli}}^{\text{LCNT}}$ in **eq. (1)**), possibly limiting the extent of the embedment.

On the other hand, at higher temperatures, exsolved particles tend to gradually rise to the surface and form the faceted interface with the LCNT. To elucidate the reason why this happened, for three different particle configurations with different embedment depth, we present each free-energy term in **eq. (1)** as well as the change in total free energy as a function of particle volume (**Fig. 3a-c**). The calculations of free energies would be complex and dependent on material and system. Hence, we choose to have a qualitative description of the key factors. The term $V_{\text{eli}}^{\text{LCNT}} \Delta g_{\text{eli}}^{\text{LCNT}}$ is set to decrease in the order of the hemisphere, intermediate, and sphere (these structures highlighted in Fig 3 insets) due to the difference in the degree of the embedment. In addition, taking into account the surface-to-volume ratio of each particle shape, we set ΔG_{area}^* to increase from the sphere to intermediate and hemisphere. To facilitate comparison among the different configurations, we also present their total free energies together in **Fig. 3d**. In **Fig. 3d**, it is seen that the total free energy of the spherical particle drops most rapidly compared to the others when the particle size is small owing to the lowest energy cost to create the surface and interface. However, $V_{\text{eli}}^{\text{LCNT}} \Delta g_{\text{eli}}^{\text{LCNT}}$ becomes significant with increasing particle volume, limiting the free energy reduction. The decrease in the embedment depth helps further reduce the free energy of a system when the particle is large despite the greater energy cost from introducing the wider surface and interface, as shown in **Fig. 3b** and

3c. Note that reducing the embedment depth does not simply mean the rise of a spherical particle. Instead, the growth of the particle toward the bulk region is suppressed, which leads to the rather flat and coherent interface (e.g., Ni(100)/LCNT(100) interface), as generally observed for nanoparticles prepared by deposition.

The final question that deserves attention is why larger particles maintain a polyhedral shape instead of adopting a hemisphere shape that has the lowest surface-to-volume ratio. According to the calculations discussed above, this seems to be due to the preference of adopting the more stable Ni(111) facets with the lowest surface energy. However, this fact cannot completely rationalize the occurrence of the non-hemisphere shapes such as the pyramid and triangular plate because they produce considerably larger surface and interface area compared to the hemisphere. To reveal the underlying reason for the formation of the polyhedral shapes with low-index facet on surface, we compare the shape factors among competing forms assuming the same volume. Here we focus on the case of pyramid vs. hemisphere grown on the LCNT(100) surface, but the conclusion drawn by this analysis is applicable to the case of triangular plate vs. sphere³⁴. Rearranging **eq. (2)** yields the equation for the shape factor as follows:

$$\alpha_{\text{shape}} = \frac{A_{\text{surf}}^{\text{Ni}} \gamma_{\text{surf}}^{\text{Ni}} + A_{\text{int}} \gamma_{\text{int}}^*}{(V^{\text{Ni}})^{\frac{2}{3}}}, \quad (3)$$

where γ_{int}^* is an effective interface energy defined as $\gamma_{\text{int}} - \gamma_{\text{surf}}^{\text{LCNT}}$. $A_{\text{surf}}^{\text{LCNT}}$ is set equal to A_{int} . Considering the surface energy of the 1.93 J/m² for the Ni(111) surface and 2.45 J/m² for the hemisphere and their geometrical information (**Table 2**), we can see that the pyramid shape can be lower in energy than the hemisphere only if γ_{int}^* is smaller than 0.917 J/m² (**Fig. 3e**). That is, for the pyramid shape to be formed, the adhesion between Ni and LCNT at the interface must be strong enough to overcome the geometrical disadvantage, namely the larger surface and interface area. To check γ_{int}^* is lower than such a critical value, we perform DFT calculations. Because of the A-site deficiency and propensity of the Ni surface segregation, we consider (TiNi)O₂- and NiO₂-terminated LCNT(100) planes when modeling the Ni-LCNT interface structure (**Supplementary Fig. 8**). We first calculate work of adhesion (W_{ad}) that is defined as:

$$W_{\text{ad}} = \frac{E(\text{Ni}) + E(\text{LCNT}) - E(\text{Ni-LCNT})}{A}, \quad (4)$$

where $E(\text{Ni})$ and $E(\text{LCNT})$ are the DFT energy of the isolated Ni and LCNT slab, respectively, $E(\text{Ni-LCNT})$

is the DFT energy of the interface model, and A is the interface area. Then, we obtain γ_{int}^* using the relation of $W_{\text{ad}} = \gamma_{\text{surf}}^{\text{Ni}} + \gamma_{\text{surf}}^{\text{LCNT}} - \gamma_{\text{int}} \cdot \gamma_{\text{int}}^*$ is calculated to be 0.02 J/m^2 and -0.12 J/m^2 when the interface includes (TiNi)O₂ and TiO₂ units, respectively. This confirms that the pyramid is indeed energetically favorable over the hemisphere.

One very important aspect to conclude from the above discussion is the key importance and exceptional interaction of the particle-support interface in these systems. As shown by our DFT calculations above, as well as Gibbs energy model and shape models, this interaction, by virtue of its epitaxy, manifests a profound and powerful effect on the exsolved particles, dictating not only the geometry of the interface but also that of the particle itself. It follows thus, that the stability of these polyhedral particles is expected to be even greater than those of spherically exsolved particles. As shown next, this is clearly substantiated through our long-term catalytic testing in very harsh hydrocarbon environment.

Shape control effect on activity and stability.

To evaluate the catalytic activity and durability of shape-controlled Ni nanoparticles, we investigate its application for a catalyst of dry reforming of methane (DRM, $\text{CO}_2 + \text{CH}_4 \leftrightarrow 2\text{CO} + 2\text{H}_2$, $\Delta H_{298\text{K}} = 247 \text{ kJ/mol}$)³⁵. **Fig 4** exhibits the CH₄ and CO₂ conversion activity of shape-controlled exsolution system and reference catalysts with same Ni contents of 7.2 wt% (**Method and Supplementary Fig. 9**). For all of catalysts, the conversion ratio of CO₂ was higher than that of CH₄ due to side reactions including reverse water-gas shift reaction ($\text{CO}_2 + \text{H}_2 \leftrightarrow \text{CO} + \text{H}_2\text{O}$, $\Delta H_{298\text{K}} = 41 \text{ kJ/mol}$). For reaction temperature of 700 °C, the oxide-supported nano-catalysts show greater initial conversion activity (above 80%) than the mixture catalyst (below 50%) because of large catalytically active surface area. However, the infiltrated Ni on ZrO₂ was quickly deactivated owing to degradation of Ni nano-catalysts such as carbon coking and agglomeration. While, the Ni-exsolved catalysts show the excellent durability through socketed structure and strong interaction between particle and support, which provide resistance for carbon coking and agglomeration on Ni nano-catalysts as mentioned previously¹. Interestingly, the activity decline of the faceted Ni on LCNT was remarkably slower compared to spherical Ni on LCNT and reference catalysts, with retaining ~83% of the initial CH₄ conversion after 140 h. During reaction at 800 °C, the Ni-exsolved catalysts exhibited the higher activity and stability than at 700 °C due to enhanced reaction kinetics and inhibition of side reaction via increasing reaction temperature. However, carbon coking persists, and high reaction temperatures

cause more thermal agglomeration and sintering of nano-catalysts. The carbon coking was observed on tested nano-catalysts, as shown in **Supplementary Fig.10**. Nevertheless, the faceted Ni exhibited high and continuous conversion activity above 94% for 390 h, while the CH₄ conversion of spherical Ni on LCNT and infiltrated Ni on ZrO₂ reduced by about 7% for 236 h, 10% for 150 h, respectively, compared to initial CH₄ conversion ratio.

In order to understand the difference in durability of nano-catalysts on DRM, the tested catalysts were investigated using TEM/EDS analysis. The carbons are formed by mainly methane decomposition ($\text{CH}_4 \leftrightarrow \text{C} + 2\text{H}_2$, $\Delta H_{298\text{K}} = 75 \text{ kJ/mol}$) and Boudouard reaction ($2\text{CO} \leftrightarrow \text{C} + \text{CO}_2$, $\Delta H_{298\text{K}} = -173.0 \text{ kJ/mol}$), and are diffused to the nanoparticle-support interface, nucleating carbon nanotubes (CNTs). The CNTs on the tested catalysts show diverse growth behaviors that imply different growth mechanisms^{1,36}. As shown by infiltrated Ni on ZrO₂ after DRM in **Supplementary Fig.11a**, the tip-growth of CNTs at interface between Ni and support can cause degradation of the Ni catalysts by separating the Ni particle from support. This tip growth occurs when interaction between metallic particle and support is weak, resulting in a sharp decline of catalytic activity. For exsolable catalysts, the Ni nanoparticles on oxide surface were well anchored with strong interaction between metallic particles and support. This unique interaction induces base-growth of CNTs without separation between Ni catalysts and support^{36,37}. The spherical Ni on LCNT was well anchored but was covered by carbon cokes, which lead to linear decline of conversion activity (**Supplementary Fig.11b**). However, the faceted Ni on LCNT exhibited more stable performance on DRM than spherical Ni on LCNT. This is due to different growth mechanism of CNTs on faceted Ni via low Ni-C binding energy on chemical absorption of flat (111) surface compared to Ni cluster³⁶. As shown in **Supplementary Fig.11c**, thus, the base-growth of CNTs on flat Ni surface tend to take an outward growth direction at interface instead of covering the surface of catalysts, keeping the activity of catalysts. This suggests that the shape evolution on high-temperature exsolution can enhance durability of the catalyst via stabilized flat, crystallographically-aligned surface and socketed structure with large interface area. Hence, the faceted Ni on LCNT shows the good reactivity and lifespan at high temperatures as compared with reported nano-catalysts with exsolution method or/and infiltration, as shown in **Supplementary Table 2**.

Conclusions

In summary, we have demonstrated that particle growth on exsolution process can induce faceted particle surface and interface between particle and support. The shape evolution mechanism was demonstrated using the thermodynamic principle for minimization of free energy. The enhanced stability of Ni catalyst supported on a perovskite oxide was achieved by high temperature exsolution with shape evolution. We expect such shape evolution of exsolved materials to have potential for tuning of performance of diverse application such as solid oxide cells, sensors, metal-air batteries and production of fuels.

Methods

Sample preparation

The perovskite materials were prepared by the conventional solid-state reaction method. A powder mixture of La_2O_3 (99.9%, Alfa aesar), TiO_2 (99.8%, Sigma-Aldrich), $\text{Ni}(\text{NO}_3)_2 \cdot 6\text{H}_2\text{O}$ (99%, Acros organics), CaCO_3 (99.5%, Alfa aesar) for designed stoichiometry and composition were mixed by a stirrer using magnetic bar and deionized (DI) water. After drying, the powder mixture was pressed into disk-shaped pellets in a steel die under a pressure of about 7 Mpa for 1min and was pre-sintered at 1000 °C for 3 h in static air condition to form perovskite phase. The pre-sintered samples were wet-milled in planetary mill using a steel jar, steel balls and DI water. The well-mixed powder mixture was pressed into disk-shaped pellets, then final-sintered at 1300 or 1500 °C for 3 h to prepare the designed perovskite material. The perovskite powders are prepared by ball-milling for 1h, with high-energy ball mill (SPEX 8000M Mixer/mill). For the Ni nanoparticles exsolution on perovskite, the pellet and powder samples were reduced by flowing dry H_2 gas with purity of 99.5% in quartz tube furnace at 600 – 1000 °C for 3 and 24 h, with heating and cooling period in pure N_2 gas with rates of 5 °C/min.

The LCNT perovskite catalyst was prepared by grinding the synthesized perovskite in planetary mill at 300 rpm for 4 h. 7.2wt% Ni/ ZrO_2 mixture and supported Ni (7.2wt%) on ZrO_2 was used for preparing reference of catalyst to compare with exsolution system. The 7.2wt% Ni/ ZrO_2 mixture was prepared by mixing the NiO powder (99.97%, Kojundo Chemical Laboratory Co., LTD.) and ZrO_2 powder (99%, ~5 μm , Sigma-Aldrich) in planetary mill at 200 rpm for 2 h. The supported Ni (7.2wt%) on ZrO_2 was prepared by infiltration method. Infiltration process was employed on the ZrO_2 powder by using an 1M aqueous solution with Ni nitrate. The concentration of urea in the precursor solution was 10 times higher than that of Ni ions to ensure good dispersion and formation of Ni nanoparticles on ZrO_2 powder. Thermal treatment was conducted at 80 °C for 2 h to decompose urea and

calcined at 400 °C for 2 h to eliminate organic compounds. The amount of Ni used for infiltration were fixed to be 7.2wt% to compare with perovskite with same amount of Ni.

Characterization

The crystalline phase of LCNT powders was identified by using High Resolution – X Ray Diffraction (HR-XRD, Rigaku SmartLab, Cu K α radiation) in the 2θ range from 20° to 90° with a step of 0.02°. The measured XRD data of LCNT powders before/after reduction were refined by rietveld analysis with GSAS software to estimate lattice information (space group, lattice parameter, etc.) and phase fraction between Ni and perovskite. The surface morphology of the perovskites pellet, catalysts before/after reduction and catalysts before/after DRM test was observed by Field Emission - Scanning Electron Microscope (FE-SEM, JEOL JSM-7001F). The lamella samples for TEM analysis are prepared from reduced perovskite surface by using Focused Ion beam (FIB, FEI Quanta 3D FEG). The crystallographic structure of exsolved Ni particles with different size/shape was analyzed by High Voltage Transmission Electron Microscopy (HVEM, JEOL JEM ARM 1300S, 1250 kV). The epitaxial relationship and d-spacing was confirmed by Fast Fourier Transition (FFT) of the HVEM images. Raman spectra was analyzed using Raman-LTPL system (Witec alpha 300). The extent of carbon coking was estimated by Thermogravimetric analysis (TGA) – Differential Scanning Calorimetry (DSC) using high temperature Simultaneous Thermal Analyzer (STA, Netzsch STA449 F3). TEM image and EDS mapping of catalysts after DRM were obtained using Field Emission – Scanning Transmission Electron Microscope (FE-STEM, Thermo Fisher Scientific Talos F200X, 200 kV).

DFT calculation

We considered orthorhombic LCNT with a composition of $\text{La}_{0.75}\text{Ca}_{0.25}\text{Ni}_{0.25}\text{Ti}_{0.75}\text{O}_3$. Density functional theory calculations were performed using Vienna *Ab initio* Simulation Package (VASP) with PAW pseudopotentials³⁸. The Perdew-Burke-Ernzerhof (PBE) functional was employed for evaluating the exchange-correlation energy³⁹. A plane-wave basis was employed with 500 eV cutoff and a 4x4x1 *k*-point grid was used for Brillouin zone integration when calculating surface and interface systems. To avoid spurious interactions between periodic images along the vertical direction within the periodic boundary condition, the vacuum with a thickness larger than 10 Å was added into every supercell. Atomic positions were relaxed until forces acting on every atom become less than 0.05 eV/Å.

Dry reforming of methane

Dry reforming of CH₄ and CO₂ were carried out in a packed bed quartz reactor system (diameter: 8 mm, length: 75 cm) where the outline was connected to a gas chromatography (GC, Younglin Acme 6000E GC) with thermal conductivity detector (TCD). He was used as a carrier gas at a constant flow rate of 20 ml min⁻¹. The temperature of column oven kept constant at 160 °C for 8 min. The temperatures of both the injector and the TCD detector were kept constant at 120 °C. The catalysts of 100 mg were loaded in the quartz reactor using quartz wool. The reactor with sample loading places in middle of furnace. To prepare the reference catalyst Ni and 7.2wt% Ni/ZrO₂ mixture, the NiO and NiO/ZrO₂ powder was reduced at 700 °C for 24 h under dry H₂ environment. The LCNT was also reduced at 700 and 900 °C for 24 h dry H₂ environment to grow spherical and faceted Ni nanoparticles, respectively. After reduction process, the DRM reaction was started in flowing feed gas of 50 ml min⁻¹ with GHSV of 30,000 mlg⁻¹h⁻¹ (CH₄:CO₂ = 1:1) at 700 and 800 °C. The conversion of CH₄ (X_{CH_4}) and CO₂ (X_{CO_2}) was calculated from measured concentration of inlet and outlet gases as follows:

$$X_{CH_4} = \frac{[CH_4]_{in} - [CH_4]_{out}}{[CH_4]_{in}}$$

$$X_{CO_2} = \frac{[CO_2]_{in} - [CO_2]_{out}}{[CO_2]_{in}}$$

References

1. Neagu, D. *et al.* Nano-socketed nickel particles with enhanced coking resistance grown in situ by redox

- exsolution. *Nature Communications* **6**, 1–8 (2015).
2. Lee, J. G. *et al.* Replacement of Ca by Ni in a Perovskite Titanate to Yield a Novel Perovskite Exsolution Architecture for Oxygen-Evolution Reactions. *Advanced Energy Materials* **10**, 1–6 (2020).
 3. Naeem, M. A. *et al.* Exsolution of Metallic Ru Nanoparticles from Defective, Fluorite-Type Solid Solutions $\text{Sm}_2\text{Ru}_{1-x}\text{Ce}_x\text{O}_7$ to Impart Stability on Dry Reforming Catalysts. *ACS Catalysis* **10**, 1923–1937 (2020).
 4. Tang, C. *et al.* Towards efficient use of noble metals: Via exsolution exemplified for CO oxidation. *Nanoscale* **11**, 16935–16944 (2019).
 5. Neagu, D. *et al.* Demonstration of chemistry at a point through restructuring and catalytic activation at anchored nanoparticles. *Nature Communications* **8**, (2017).
 6. Sun, Y. F. *et al.* Toward a rational photocatalyst design: A new formation strategy of co-catalyst/semiconductor heterostructures: Via in situ exsolution. *Chemical Communications* **54**, 1505–1508 (2018).
 7. Myung, J. H., Neagu, D., Miller, D. N. & Irvine, J. T. S. Switching on electrocatalytic activity in solid oxide cells. *Nature* **537**, 528–531 (2016).
 8. Park, S. *et al.* In situ exsolved Co nanoparticles on Ruddlesden-Popper material as highly active catalyst for CO₂ electrolysis to CO. *Applied Catalysis B: Environmental* **248**, 147–156 (2019).
 9. Sun, Y. *et al.* A-site deficient perovskite: The parent for in situ exsolution of highly active, regenerable nano-particles as SOFC anodes. *Journal of Materials Chemistry A* **3**, 11048–11056 (2015).
 10. Duan, C. *et al.* Highly durable, coking and sulfur tolerant, fuel-flexible protonic ceramic fuel cells. *Nature* **557**, 217–222 (2018).
 11. Jo, S., Jeong, H. G., Kim, Y. H., Neagu, D. & Myung, J. Stability and Activity Controls of Cu Nanoparticles for High-performance Solid Oxide Fuel Cells. *Applied Catalysis B: Environmental* **285**, 119828 (2020).
 12. Otto, S. K. *et al.* Exsolved Nickel Nanoparticles Acting as Oxygen Storage Reservoirs and Active Sites

- for Redox CH₄ Conversion. *ACS Applied Energy Materials* **2**, 7288–7298 (2019).
13. Cong, Y. *et al.* Cation Segregation of A-Site Deficiency Perovskite La_{0.85}FeO_{3-δ} Nanoparticles toward High-Performance Cathode Catalysts for Rechargeable Li-O₂ Battery. *ACS Applied Materials and Interfaces* **10**, 25465–25472 (2018).
 14. Sun, Y. & Xia, Y. Shape-controlled synthesis of gold and silver nanoparticles. *Science* **298**, 2176–2179 (2002).
 15. Neagu, D., Tsekouras, G., Miller, D. N., Ménard, H. & Irvine, J. T. S. In situ growth of nanoparticles through control of non-stoichiometry. *Nature Chemistry* **5**, 916–923 (2013).
 16. Kim, K. J. *et al.* Facet-Dependent in Situ Growth of Nanoparticles in Epitaxial Thin Films: The Role of Interfacial Energy. *Journal of the American Chemical Society* **141**, 7509–7517 (2019).
 17. Gao, Y. *et al.* Energetics of Nanoparticle Exsolution from Perovskite Oxides. *Journal of Physical Chemistry Letters* **9**, 3772–3778 (2018).
 18. Zeng, D. *et al.* Enhanced hydrogen production performance through controllable redox exsolution within CoFeAlO: X spinel oxygen carrier materials. *Journal of Materials Chemistry A* **6**, 11306–11316 (2018).
 19. Kim, J. K. *et al.* Exceptional Tunability over Size and Density of Spontaneously Formed Nanoparticles via Nucleation Dynamics. *ACS Applied Materials & Interfaces* (2020).
 20. Kousi, K., Neagu, D., Bekris, L., Papaioannou, E. I. & Metcalfe, I. S. Endogenous Nanoparticles Strain Perovskite Host Lattice Providing Oxygen Capacity and Driving Oxygen Exchange and CH₄ Conversion to Syngas. *Angewandte Chemie - International Edition* **59**, 2510–2519 (2020).
 21. Neagu, D. *et al.* In Situ Observation of Nanoparticle Exsolution from Perovskite Oxides: From Atomic Scale Mechanistic Insight to Nanostructure Tailoring. *ACS Nano* **13**, 12996–13005 (2019).
 22. Wang, Y. *et al.* Exsolved Fe-Ni nano-particles from Sr₂Fe_{1.3}Ni_{0.2}Mo_{0.5}O₆ perovskite oxide as a cathode for solid oxide steam electrolysis cells. *Journal of Materials Chemistry A* **4**, 14163–14169 (2016).

23. Jo, Y. R. *et al.* Growth Kinetics of Individual Co Particles Ex-solved on SrTi_{0.75}Co_{0.25}O_{3-d} Polycrystalline Perovskite Thin Films. *Journal of the American Chemical Society* **141**, 6690–6697 (2019).
24. Zubenko, D., Singh, S. & Rosen, B. A. Exsolution of Re-alloy catalysts with enhanced stability for methane dry reforming. *Applied Catalysis B: Environmental* **209**, 711–719 (2017).
25. Zhu, T., Troiani, H. E., Mogni, L. V., Han, M. & Barnett, S. A. Ni-Substituted Sr(Ti,Fe)O₃ SOFC Anodes: Achieving High Performance via Metal Alloy Nanoparticle Exsolution. *Joule* **2**, 478–496 (2018).
26. Gao, Y., Chen, D., Saccoccio, M., Lu, Z. & Ciucci, F. From material design to mechanism study: Nanoscale Ni exsolution on a highly active A-site deficient anode material for solid oxide fuel cells. *Nano Energy* **27**, 499–508 (2016).
27. Oh, J. H. *et al.* Importance of Exsolution in Transition-Metal (Co, Rh, and Ir)-Doped LaCrO₃ Perovskite Catalysts for Boosting Dry Reforming of CH₄ Using CO₂ for Hydrogen Production. *Industrial and Engineering Chemistry Research* **58**, 6385–6393 (2019).
28. Mittendorfer, F., Eichler, A. & Hafner, J. Structural, electronic and magnetic properties of nickel surfaces. *Surface Science* **423**, 1–11 (1999).
29. Wang, Z. L. Transmission electron microscopy of shape-controlled nanocrystals and their assemblies. *Journal of Physical Chemistry B* **104**, 1153–1175 (2000).
30. An, K. & Somorjai, G. A. Size and Shape Control of Metal Nanoparticles for Reaction Selectivity in Catalysis. *ChemCatChem* **4**, 1512–1524 (2012).
31. Silly, F., Powell, A. C., Martin, M. G. & Castell, M. R. Growth shapes of supported Pd nanocrystals on SrTiO₃(001). *Physical Review B - Condensed Matter and Materials Physics* **72**, 1–6 (2005).
32. Winterbottom, W. L. Equilibrium shape of a small particle in contact with a foreign substrate. *Acta Metallurgica* **15**, 303–310 (1967).
33. Silly, F. & Castell, M. R. Selecting the shape of supported metal nanocrystals: Pd Huts, hexagons, or

- pyramids on SrTiO₃(001). *Physical Review Letters* **94**, 3–6 (2005).
34. Deivaraj, T. C., Lala, N. L. & Lee, J. Y. Solvent-induced shape evolution of PVP protected spherical silver nanoparticles into triangular nanoplates and nanorods. *Journal of Colloid and Interface Science* **289**, 402–409 (2005).
35. Abdullah, B., Abd Ghani, N. A. & Vo, D. V. N. Recent advances in dry reforming of methane over Ni-based catalysts. *Journal of Cleaner Production* **162**, 170–185 (2017).
36. Gohier, A., Ewels, C. P., Minea, T. M. & Djouadi, M. A. Carbon nanotube growth mechanism switches from tip- to base-growth with decreasing catalyst particle size. *Carbon* **46**, 1331–1338 (2008).
37. Dijon, J. *et al.* How to switch from a tip to base growth mechanism in carbon nanotube growth by catalytic chemical vapour deposition. *Carbon* **48**, 3953–3963 (2010).
38. Kresse, G. & Furthmüller, J. Efficient iterative schemes for ab initio total-energy calculations using a plane-wave basis set. *PHYSICAL REVIEW B* **54**, 11169–11186 (1996).
39. Perdew, J. P., Burke, K. & Ernzerhof, M. Generalized gradient approximation made simple. *Physical Review Letters* **77**, 3865–3868 (1996).

Acknowledgement

This work was supported by National Research Foundation of Korea (NRF-2018R1C1B5044487) and (NRF-2019R1G1A1009363). The HVEM measurements were supported by the KBSI R&D program (Project No. C030440). D.N. gratefully acknowledges the Royal Society for the grant RGS/R1/211253.

Author contribution

Y.H.K. designed the experiments, analyzed the data and wrote the paper with assistance from D.N. and Y.K. Y.H.K., S.J and H.J performed the experiments. Y.K. performed DFT calculation. J.M. conceived, supervised and led the project. All authors discussed the results and commented on the manuscript.

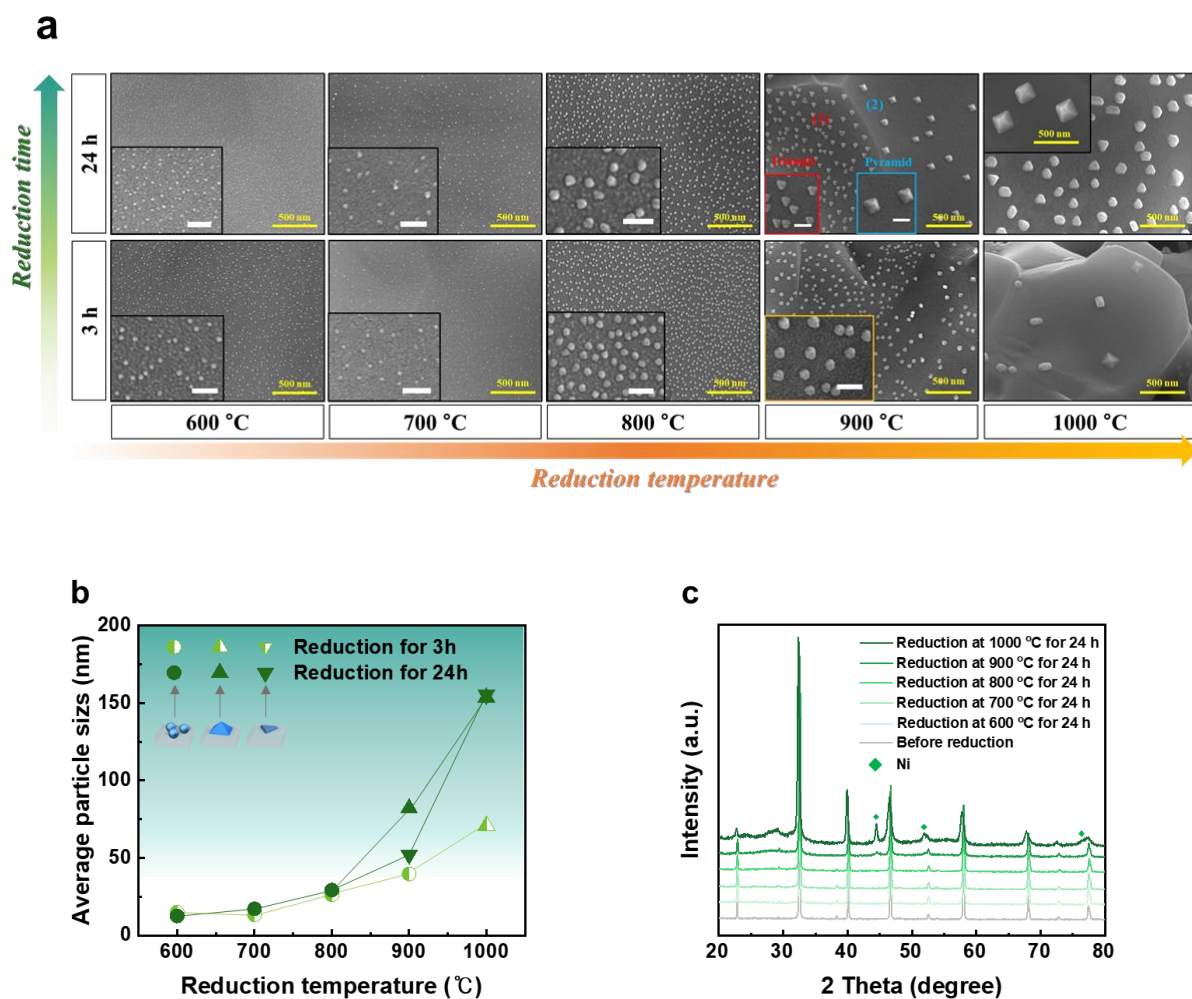


Figure 1. Ni nanoparticle growth on LCNT perovskite with shape change. a. Surface morphology of LCNT reduced in dry H₂ at 600 – 1000 °C for 3 h and 24 h; White scale bar, 100 nm. **b.** Particle size and temperature dependence of shape evolution; Spherical shape (●), triangular plate (▼) and pyramid (▲). **c.** XRD patterns of LCNT before/after reduction in dry H₂ at 600 – 1000 °C for 24 h.

Table 1: Detail in exsolved particle analysis.

Reduction temperature (°C)	Reduction time (h)	Average particle size (nm)	Particle shape	Population density (μm^{-2})	Area coverage (%)
600	3	14.86	Sph	228.28	4.1
	24	12.52	Sph	597.59	7.7
700	3	13.23	Sph	173.36	2.5
	24	17.10	Sph	178.35	4.3
800	3	26.24	Sph	301.77	16.5
	24	29.20	Sph	217.35	14.7
900	3	39.63	Sph	77.05	9.7
	24	52.06	Tri	72.41	15.5
		81.96	Pyr	4.04	2.1
1000	3	70.84	Pyr	2.63	2.8
	24	155.32	Tri	13.79	16.4
		153.61	Pyr	3.19	10.3

*Sph, Tri and Pry represent sphere, triangular plate and pyramid.

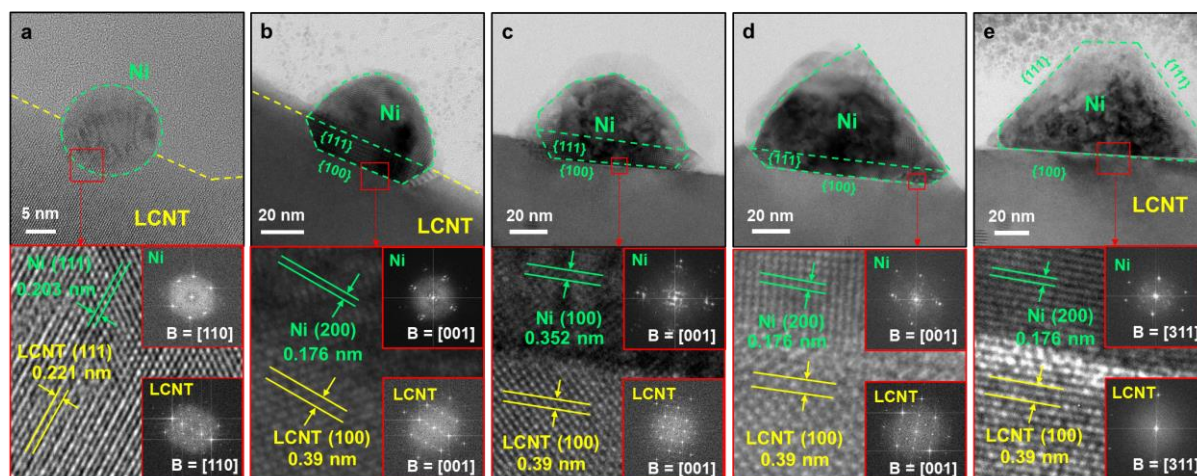


Figure 2. HVEM images with fast Fourier transform (FFT) of exsolved Ni particles with different size. (a) The spherical nickel nanoparticle on LCNT powder reduced at 800 °C for 24 h, and (b-e) the polyhedral nickel nanoparticles with different size and shape, on lamella sample from LCNT pellets reduced at 900 °C for 3 h or 24 h.

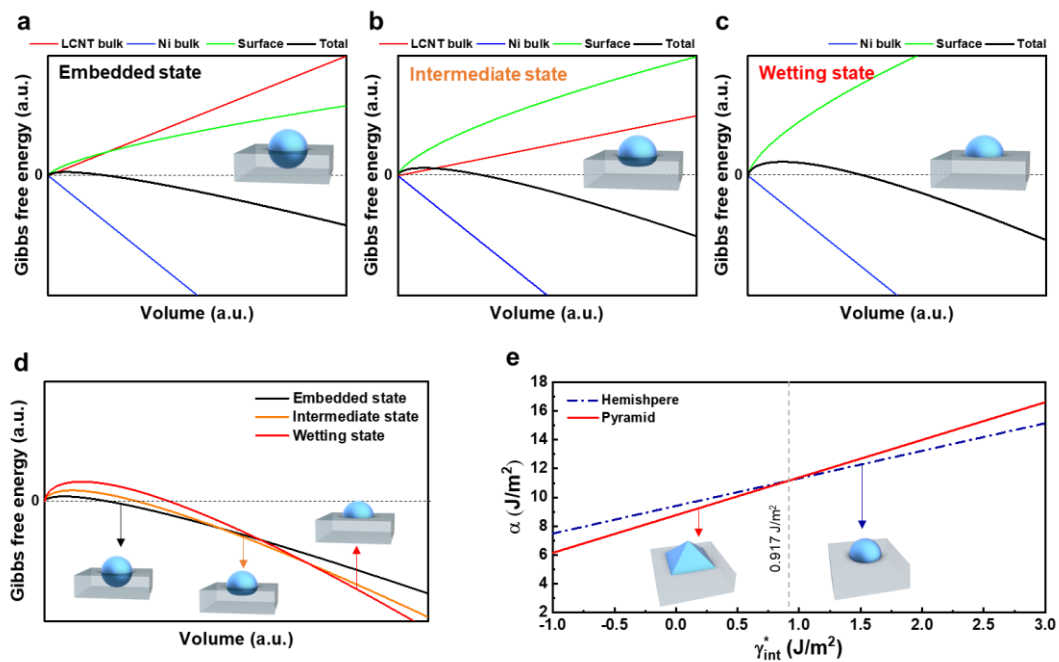
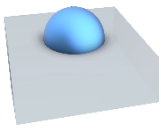
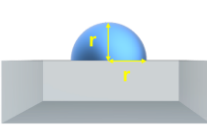
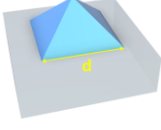
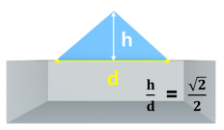


Figure 3. Shape formation mechanism of exsolved Ni on LCNT. Gibbs free energy for Ni exsolution in **a.** embedded state, **b.** intermediate state and **c.** wetting state. **d.** comparison of Gibbs free energy. **e.** the shape factors (α_{shape}) of the equilibrium shapes for the interface energy – dependence.

Table 2. Detail in shape factor calculation with wetting shapes on perovskite (100) surface.

Wetting shapes	Hemisphere		Pyramid	
	Left side view	Front view	Left side view	Front view
				
Interface area (A_{int})	πr^2		d^2	
Surface area (A_{sur})	$2\pi r^2$		$\sqrt{3}d^2$	
Volume ($V_{Ni\ bulk}$)	$(2/3)\pi r^3$		$(\sqrt{2}/6)d^3$	
surface energy of bulk Ni (γ_{sur})	2.45 J/m ² (poly-crystal) [ref.28]		1.93 J/m ² ({111} facet) [ref.28]	
Shape factor (α_{shape})	$\alpha_{hemisphere} = (18\pi)^{\frac{1}{3}}\gamma_{sur} + (\frac{9}{4}\pi)^{\frac{1}{3}}\gamma_{int}^*$		$\alpha_{pyramid} = (54\sqrt{3})^{\frac{1}{3}}\gamma_{sur} + (18)^{\frac{1}{3}}\gamma_{int}^*$	

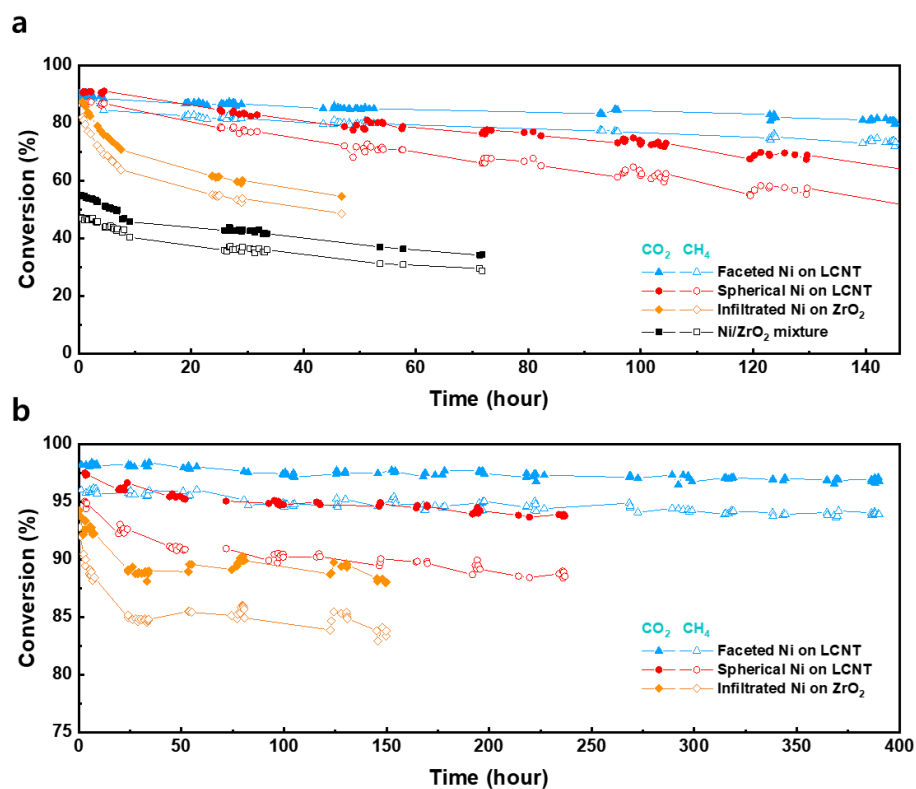


Figure 4. Activity of shape-controlled Ni exsolution and reference catalysts in dry reforming of methane.

Continuous catalytic reaction of CH₄ and CO₂ at reaction temperatures of **a.** 700 °C and **b.** 800 °C (GHSV = 30000 mlg⁻¹h⁻¹).